Available online at www.sciencedirect.com
ScienceDirect
Trans. Nonferrous Met. Soc. China 33(2023) 743−754
Transactions of Nonferrous Metals Society of China
www.tnmsc.cn

Corrosion behavior and mechanical properties of extruded low-alloyed Mg−0.5Bi−0.5Y−0.2Zn alloy

Feng LI[1], Wei-li CHENG[1,2], Hui YU[3], Hong-xia WANG[1,2], Xiao-feng NIU[1,2], Li-fei WANG[1,2], Hang LI[1], Hua HOU[4]

1. School of Materials Science and Engineering, Taiyuan University of Technology, Taiyuan 030024, China;
2. Key Laboratory of Interface Science and Engineering in Advanced Materials, Ministry of Education, Taiyuan University of Technology, Taiyuan 030024, China;
3. School of Materials Science and Engineering, Hebei University of Technology, Tianjin 300132, China;
4. School of Materials Science and Engineering, North University of China, Taiyuan 030051, China

Received 2 November 2021; accepted 3 March 2022

Abstract: A novel low-alloyed Mg−Bi−Y−Zn alloy system was developed and extruded successfully at 673 K. The corrosion behavior and tensile properties of the extruded alloy were investigated through scanning electron microscopy (SEM), electron backscatter diffraction (EBSD), electrochemical tests and tensile test. The extruded alloy exhibits a nearly fully recrystallized grain structure with a scattered extrusion fiber texture and some sub-micron precipitates. In SBF solution, the dominated corrosion mode changed from galvanic induced pitting corrosion at initial stage to filiform-like corrosion and finally mixed pitting corrosion and local fall-off of grains during long-term corrosion processes. The tensile properties and corrosion resistance of the extruded Mg−0.5Bi−0.5Y−0.2Zn (wt.%) alloy are: tensile yield strength of 237 MPa, ultimate tensile strength of 304 MPa, elongation to failure of 31% and mean corrosion rate of 0.14 mm/a. The great balance between tensile properties and corrosion resistance is mainly attributed to the homogeneous grain structure and the presence of sub-micron scaled precipitates, indicating a promising potential in the application in biomedical field.

Key words: Mg−Bi-based alloy; extrusion; corrosion behavior; mechanical properties

1 Introduction

Mg alloys have a similar elastic modulus to the human bone that can effectively reduce the stress shielding effect, excellent biocompatibility, mechanical compatibility and biodegradability [1−3]. However, conventional Mg alloys exhibit a relatively poor balance between strength and ductility as well as corrosion rate, which has greatly blocked their extensive application in engineering and biomedical fields [4−7]. Therefore, it is an urgent challenge to simultaneously improve the mechanical and anti-corrosion properties of Mg alloys.

Alloying can effectively modify the microstructure, strength, and corrosion behavior of Mg alloys [8−11]. Mg−Bi-based alloys with thermally stable Mg_3Bi_2 phase are promising candidates to be developed as high strength and ductility as well as excellent corrosion resistant biomedical Mg alloys [12,13]. MENG et al [14] reported a micro-alloying Mg−Bi-based alloy that exhibits an outstanding tensile elongation of 0.43 at room temperature, which is attributed to the refined grain microstructure through grain-boundary pinning effect of nano-scaled Mg_3Bi_2 and micro-scale Mg_2Bi_2Ca phases as well as the weakened $\langle 2\bar{1}\bar{1}2\rangle$ // extrusion direction (ED) texture. Similarly, the high-speed extruded Mg−5Bi−3Al alloy possessed a

Corresponding author: Wei-li CHENG, E-mail: chengweili7@126.com
DOI: 10.1016/S1003-6326(23)66142-4

higher tensile yield strength (TYS) without any loss of ductility owing to the formation of numerous Mg_3Bi_2 phase along the $\langle 0110\rangle_{Mg}$ direction during subsequent aging [15]. Furthermore, TOK et al [16] demonstrated that the Mg−1.2Ca−*x*Bi alloys present excellent corrosion resistance with the Bi addition of 0.5 wt.%, while further Bi addition from 1.5 to 12 wt.% accelerated the degradation rate due to the significant micro-galvanic effect. In addition, our previous works [17,18] validated that the corrosion rate of Mg−0.5Bi-based alloy presents relatively low corrosion rate of ~0.59 mm/a. Therefore, low-alloyed Mg−0.5Bi alloy system was selected as the base alloy in this study.

Element yttrium (Y), with a standard electrode potential equal to that of Mg (−2.732 V), can significantly refine the grain size, induce the formation of second phase particles in the matrix and Y_2O_3 protective film [19,20], which are conducive to improve the mechanical properties and corrosion resistance of the alloys simultaneously. However, high Y alloying will deteriorate the corrosion resistance due to the severe micro-galvanic corrosion. In addition, previous study [21] reported that adding Zn to Mg alloys can promote solid solution strengthening and precipitation strengthening. Besides, Zn can effectively improve the tolerance of trace impurities, such as Fe and Ni, and then effectively reduce the occurrence of galvanic corrosion. Previous studies showed that excessive Zn led to the accelerated degradation of Mg alloys [22,23]. Therefore, low content Y and Zn are selected as alloying elements to further modify the microstructure and tailor the properties of the present Mg−0.5Bi-based alloy system.

The purpose of the present study is to develop an extruded low-alloyed Mg−0.5Bi−0.5Y−0.2Zn alloy, which possesses a proper balance between tensile properties and corrosion resistance. The microstructural characteristics and the resultant corrosion behavior and tensile properties of the extruded alloy are investigated in detail.

2 Experimental

2.1 Material preparation

Mg−0.5Bi−0.5Y−0.2Zn (wt.%) (BWZ000) alloy was prepared by melting pure Mg, Bi, Zn and Mg−30wt.%Y in an electric resistance furnace under the protection gas composed of SF_6 and CO_2. The molten alloy was heated at 1023 K for 20 min and then cast at 993 K into a steel mold preheated at 473 K. Then, the cast ingot was homogenized (593 K for 1 h and 773 K for 24 h), followed by water-quenching, and finally, hot extrusion was carried out under an extrusion ratio of 25:1 and extrusion temperature of 673 K.

2.2 Microstructure observation

The microstructural characterization of the extruded alloy was carried out using scanning electron microscopy (SEM) and electron back-scatter diffraction (EBSD). The Nano Measurer 1.2 software was used to measure the average grain size. Phase composition was detected by X-ray diffractometer (XRD) and the scanning angle was 10°−80°.

2.3 Corrosion measurements

All corrosion tests in this study were performed in SBF solution. Hydrogen evolution test was performed by immersing the sample at 37 ℃ and collected hydrogen was used to calculate the corrosion rate (P_i) by the following equation [17]:

$$P_i=2.279V_H \quad (1)$$

where V_H is the average volume of H_2 produced per day on a sample surface with an area of 1 cm^2.

The electrochemical tests including potentio-dynamic polarization (PDP) test and electrochemical impedance spectroscopy (EIS) test were carried out at room temperature using an electrochemical workstation, and 8 valid samples were tested for each alloy in order to ensure the authenticity of the data.

The corrosion morphologies of the samples with and without corrosion products were observed by SEM. The samples were immersed for various time and the corrosion products were cleaned by 20 mg/mL H_2CrO_4 solution in ultrasonic wave. Then, the composition of corrosion products was determined by X-ray photoelectron spectroscopy (XPS).

2.4 Tensile properties measurements

The tensile properties of the extruded alloy, including ultimate tensile strength (UTS), tensile yield strength (TYS) and elongation (EL), were tested on an INSTRON5982 electronic universal testing machine, and samples with dimensions of

3.5 mm in width, 2 mm in thickness, and 15 mm in gauge length were tested at strain rate of 0.001 s^{-1}. Three samples of the studied alloy were prepared for testing to ensure the accuracy and stability of the experiment.

3 Results and discussion

3.1 Microstructural characterization

Figure 1 shows the EBSD orientation map in the ED−TD plane, (0001) pole figure and grain size distribution map of the extruded alloy. The microstructure of BWZ000 alloy is mainly composed of dynamic recrystallized (DRXed) grains with an average grain size (AGS) of (10.55±1.06) μm. As shown, certain extensile twins with a volume fraction of about 17.39% could be observed in the extruded BWZ000 alloy, which may be produced by relieving stress concentration during extrusion. LIU et al [24] conducted the scanning Kelvin probe force microscopy (SKPFM) to analyze the potential difference between Mg matrix and twins, and the results showed that the area with twins exhibited more negative potential than Mg matrix. Thus, the existence of twins can also induce the micro-galvanic corrosion. As can be seen from the polar diagram (Fig. 1(b)), the studied alloy presents a typical extrusion texture with the base plane parallel to the ED and the maximum texture intensity is 7.39.

SEM micrographs and XRD pattern of the extruded alloy are shown in Fig. 2. As indicated, some submicron-scaled particles mainly distributed in the grain interior rather than the grain boundary could be observed. According to the EDS spectra and map of enlarged view, the second phase was mainly composed of Mg, Bi and Y elements, which corresponded to the peaks of 29° and 42° in XRD pattern.

3.2 Corrosion resistance

Figure 3(a) presents the hydrogen volume evolution record and the hydrogen evolution rate for the studied alloy immersed in SBF solution at 37 ℃. According to the slope of curve, we divide the hydrogen evolution process into three stages. At Stage I, the hydrogen evolution rate increases nearly linearly with prolonging immersion time, which implies that the activation of the micro-galvanic corrosion is related to presence of twinning area with higher energy and certain grain regions with lower atom density. At Stage II, the slope of hydrogen evolution curve tends to be stable, which is attributed to the dynamic balance between the regeneration and break-down of corrosion product film. Prolonged immersion time (Stage III) results in a dramatically increased slope in hydrogen evolution curve, corresponding to a calculated corrosion rate of 3.617 mm/a, which demonstrates the weak protection of corrosion products film.

3.3 Electrochemical performance

Figure 4 shows anode and cathode branches of polarization curves, corresponding φ_{corr} (φ_{corr} is the corrosion potential) and P_i curves of the extruded alloy immersed in SBF solution for various time. As for anode branch, obvious pseudo-passivation could be observed when the immersing time reaches 36 h. Previous reports [4,8,25] have explained that this phenomenon is related to the formation of protective product film. Meanwhile, the value of φ_{corr} at 36 h (−1.35 V (vs SCE)) is more positive than that at 0.5 h (−1.53 V (vs SCE)) and 168 h (−1.44 V (vs SCE)), implying a weaker electrochemical activation. The cathode branch in the polarization curve is related to the hydrogen evolution process of the alloy [26]. It can be seen that, the cathode branch slope, namely hydrogen

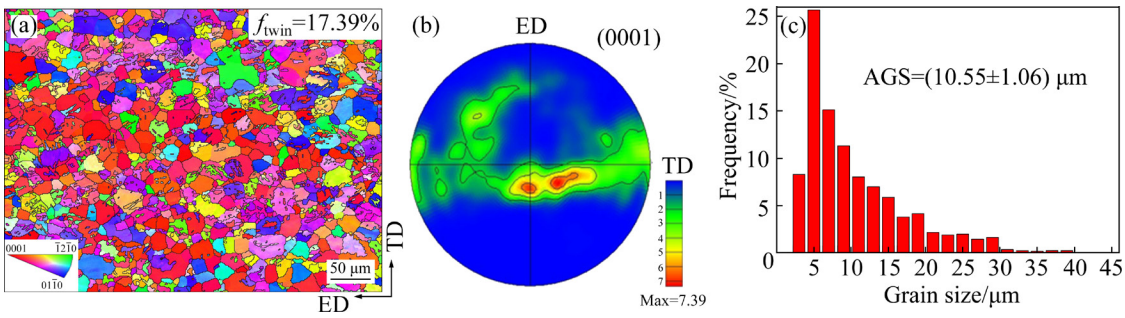

Fig. 1 EBSD orientation map in ED−TD plane (a), (0001) pole figure (b) and grain size distribution map (c) of extruded Mg−0.5Bi−0.5Y−0.2Zn alloy

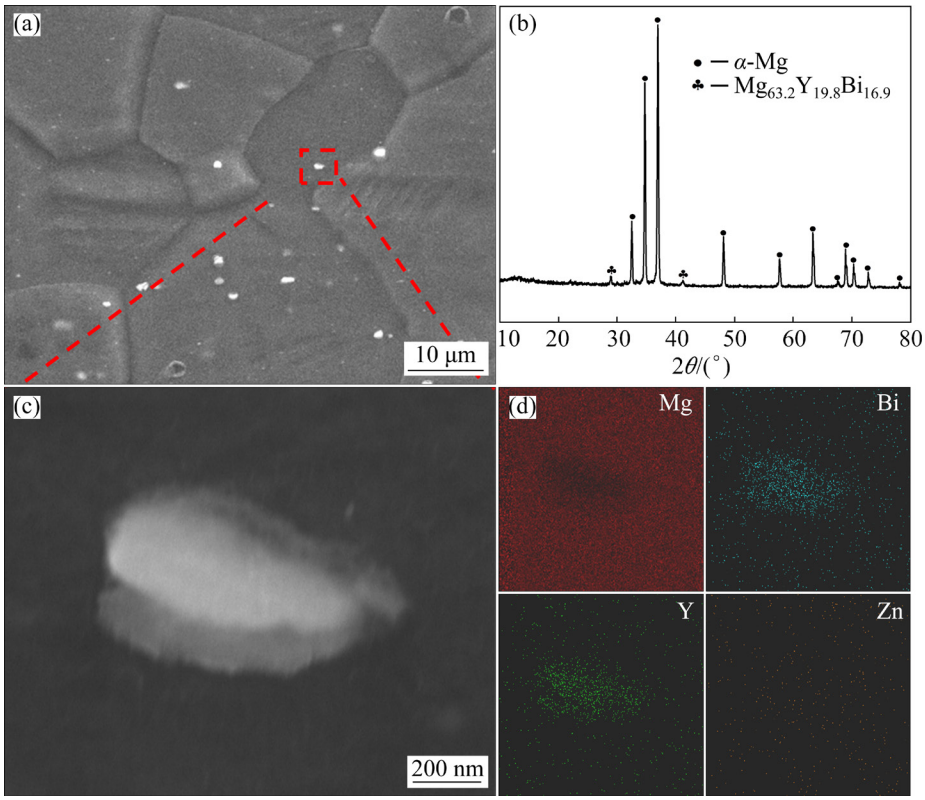

Fig. 2 SEM micrograph (a), XRD pattern (b) of extruded Mg−0.5Bi−0.5Y−0.2Zn alloy, enlarged view of second phase with EDS spectra (c) and corresponding EDS maps for second phase (d)

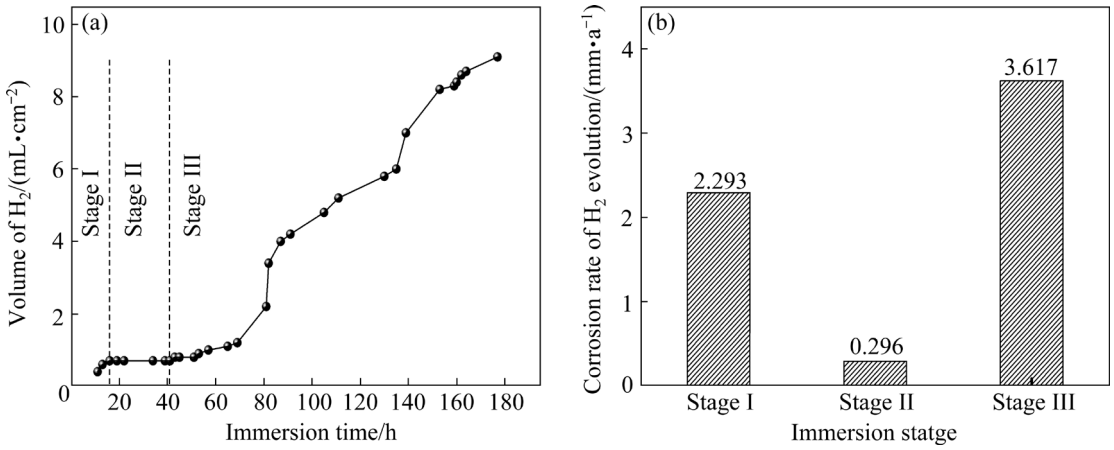

Fig. 3 Hydrogen volume evolution (a) and corresponding corrosion rate (b) of studied alloy after immersing in SBF solution at 37 ℃ for 180 h

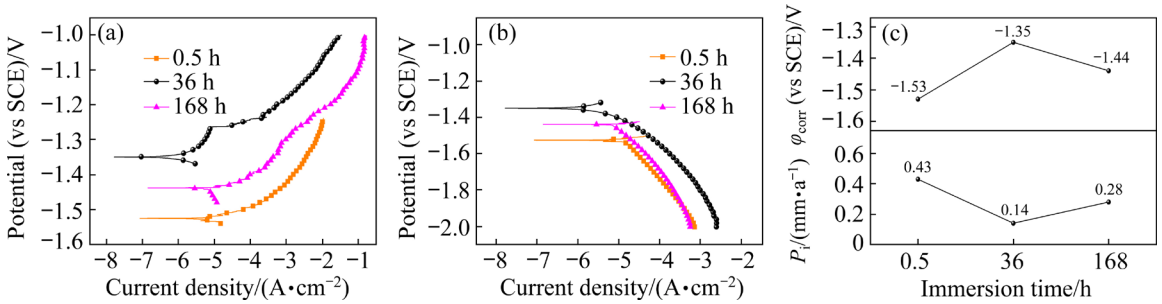

Fig. 4 Anode (a), cathode (b) branches of polarization curves, and φ_{corr} and P_i curves (c) of extruded Mg−0.5Bi−0.5Y−0.2Zn alloy after immersing in SBF solution for 0.5, 36 and 168 h

evolution rate, firstly increases and then decreases with the increased immersion time. In order to further study the corrosion performance of the studied alloy for various time, the corrosion rate P_i was calculated by the following equation [27]:

$$P_i=22.85CJ_{corr} \quad (2)$$

where C is a constant taken as 0.1 cm^3/(mA·a), and J_{corr} is the corrosion current density and is obtained by polarization curve fitting and the fitting results are shown in Table 1. As the immersion time is 36 h, the lowest value of P_i (0.14 mm/a) could be obtained.

Table 1 Fitting results of polarization curves for BWZ2000 alloy

Immersion time/h	β_a/mV	β_c/mV	J_{corr}/(mA·cm^{-2})
0.5	10.37	241.00	1.90×10^{-2}
36	30.95	161.70	6.29×10^{-3}
168	96.98	287.46	1.24×10^{-2}

β_a and β_c are the Tafel constants of anode and cathode, respectively

Figure 5(a) illustrates the Nyquist plots of the extruded alloy in SBF solution for 0.5, 36 and 168 h. During the short time immersion (0.5 h), the extruded alloy exhibits a capacitance circuit representing the charge transfer process in high frequency region, a capacitance circuit representing the product film formation process in intermediate frequency region and a low frequency inductive loop attributing to the relaxation of the adsorbed material on the surface of α-Mg matrix. And two wave peaks can be observed in the Bode plot of phase angle versus frequency as shown in Fig. 5(b). As the immersing time reaches 36 h, the low frequency loop of the alloy disappears and the dimension of the capacitor loop increases, which is related to the reduction of the active area on the alloy surface due to the formation of the passive film. With further increase in immersing time to 168 h, the reappearance of the low frequency loop manifests that the protective corrosion product film deteriorates, which reflects the increase of corrosion rate. Additionally, a large impedance modulus $|Z|$

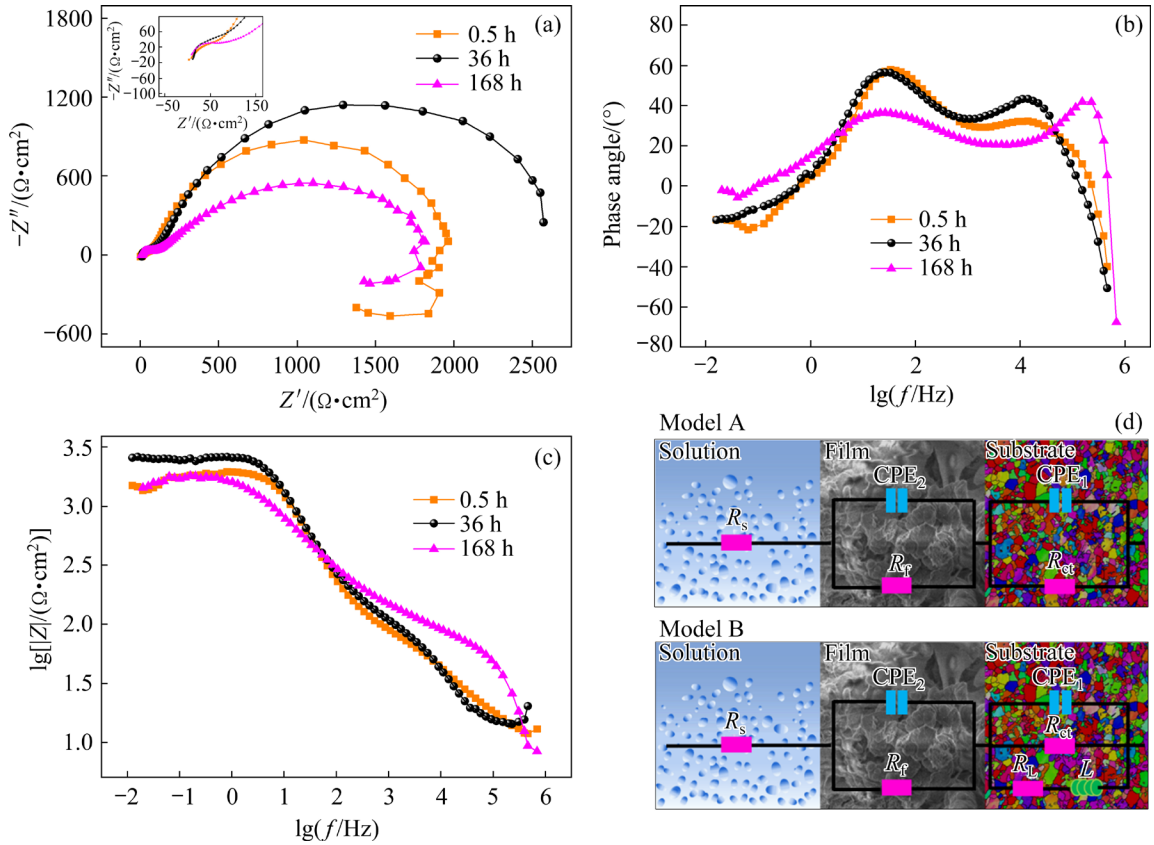

Fig. 5 Nyquist plots showing electrochemical impedance spectroscopy (EIS) with plots of local area appended on upper left corner (a), Bode plot of phase angle versus frequency (b), and Bode plot of impedance versus frequency (c) for extruded alloy measured in SBF solution at room temperature for 0.5, 36 and 168 h, and equivalent circuits (d) used to fit the EIS spectra

reflects better corrosion resistance. As shown in Fig. 5(c), the alloy after immersion for 36 h has the maximum $|Z|$ value.

The equivalent circuits in Fig. 5(d) are used for characterizing the above-mentioned interfacial processes. In the circuits, R_s, R_{ct}, R_f and R_L are the solution resistance, charge transfer resistance, film resistance and inductance resistance, respectively. CPE_1 and CPE_2 are the capacitances of double layer and products film, respectively. L is the inductance. The corresponding fitting results are listed in Table 2. As seen, the R_f of BWZ000 alloy reaches the maximum at 36 h (2536 Ω·cm^2) compared with 0.5 h (1890 Ω·cm^2) and 168 h (1710 Ω·cm^2), which implies that the protection of the product film is enhanced after immersion for 36 h. The polarization resistance (R_p) is usually used to describe the corrosion resistance of the alloy, and the value of R_p could be calculated by the following equations [8]:

$$\text{Model A: } R_p=R_s+R_f+R_{ct} \quad (3)$$

$$\text{Model B: } R_p=R_s+R_f+\left(\frac{R_{ct}R_L}{R_{ct}+R_L}\right) \quad (4)$$

The R_p value of the BWZ000 alloy increases firstly from 2114.49 to 2792.39 Ω·cm^2 and then decreases to 2303.03 Ω·cm^2. This phenomenon reflects that the corrosion resistance of the studied alloy increases when immersing for 36 h, and then deteriorates after long-time immersion, which is accordant with the hydrogen evolution and polarization curve results. Details will be discussed later.

3.4 Corrosion morphology

Figure 6 shows SEM micrographs of the studied alloy with corrosion products after immersion

Table 2 Fitting results of EIS spectra for BWZ2000 alloy

Immersion time/h	R_s/ (Ω·cm^2)	R_{ct}/ (Ω·cm^2)	CPE_1/ (F·cm^{-2})	n_1	R_f/ (Ω·cm^2)	CPE_2/ (F·cm^{-2})	n_2	R_L/ (Ω·cm^2)	L/ (H·cm^2)	R_p/ (Ω·cm^2)
0.5	13.14	126.3	2.07×10^{-5}	0.65	1890	1.22×10^{-5}	0.95	1880	14027	2114.49
36	10.99	181.4	1.62×10^{-5}	0.71	2536	1.44×10^{-5}	0.91	–	–	2792.39
168	13.98	62.24	2.73×10^{-8}	0.96	1710	1.1×10^{-4}	0.53	–	–	2303.03

n_1 and n_2 are the dispersion coefficients of CPE_1 and CPE_2, respectively

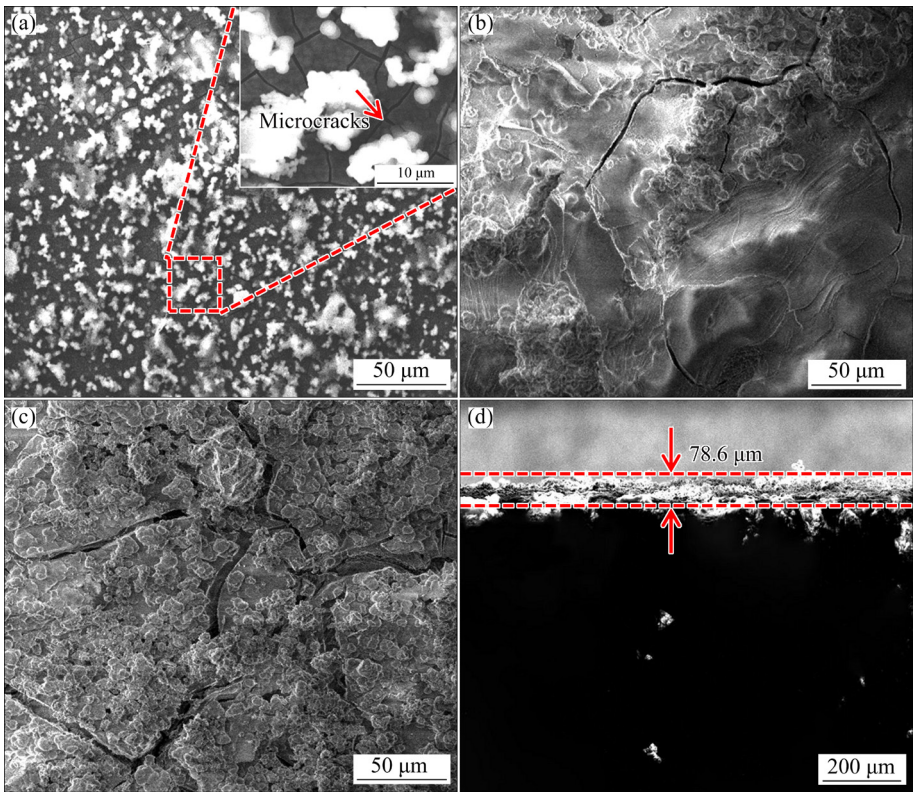

Fig. 6 Surface SEM micrographs of BWZ000 alloy with corrosion products after immersing in SBF solution for 0.5 h (a), 36 h (b), 168 h (c) and cross-section micrograph of studied alloy with corrosion products after immersing in SBF solution for 168 h (d)

for different time. As indicated, during short time immersion of 0.5 h, some loose flocculent corrosion products stack on the surface with some micro-cracks in the α-Mg. As the immersion time increases to 36 h, the corrosion products completely cover the substrate and the density of the product film is significantly improved, although some microcracks are still visible on the surface, which indicates that protective corrosion products are formed at this stage. With the immersion time extending to 168 h, corrosion product film is ruptured due to the presence of a great number of widened and deepened network cracks on the surface. This phenomenon is mainly due to the hydrogen generated in corrosion pit breaking through the oxide layer. Meanwhile, the thickness of the corrosion product film was measured after immersion for 168 h. The result shows that the product layer thickness of the studied alloy reaches 78.6 μm. The protective effect of product film with wide and deep cracks is extremely weak during this period, so the thicker product layer represents the higher matrix dissolution.

According to the XPS spectrum analysis results of the corrosion products (Fig. 7), the peak values of the high-resolution spectra for Mg 1s of the studied alloy for different time both locate at 1307.2 eV, corresponding to $Mg(OH)_2$. The peaks of Ca 2p are the same for 0.5 and 36 h, determined as $Ca(OH)_2$ in the binding energy table, which is mainly originated from the Ca^{2+} in SBF solution. After immersion for 36 h, the O 1s spectrum of alloy could be separated into two peaks with banding energy of 531.5 and 533.3 eV, which correspond to OH^- and O^{2-}, respectively. However, the corrosion products contain only OH^- after immersion for 0.5 h. The corrosion process could be expressed by the following reactions [13]:

$$Mg \rightarrow Mg^{2+}+2e \quad (5)$$

$$2H_2O+2e \rightarrow 2OH^-+H_2\uparrow \quad (6)$$

$$Mg^{2+}+2OH^- \rightarrow Mg(OH)_2 \quad (7)$$

$$Ca^{2+}+2OH^- \rightarrow Ca(OH)_2 \quad (8)$$

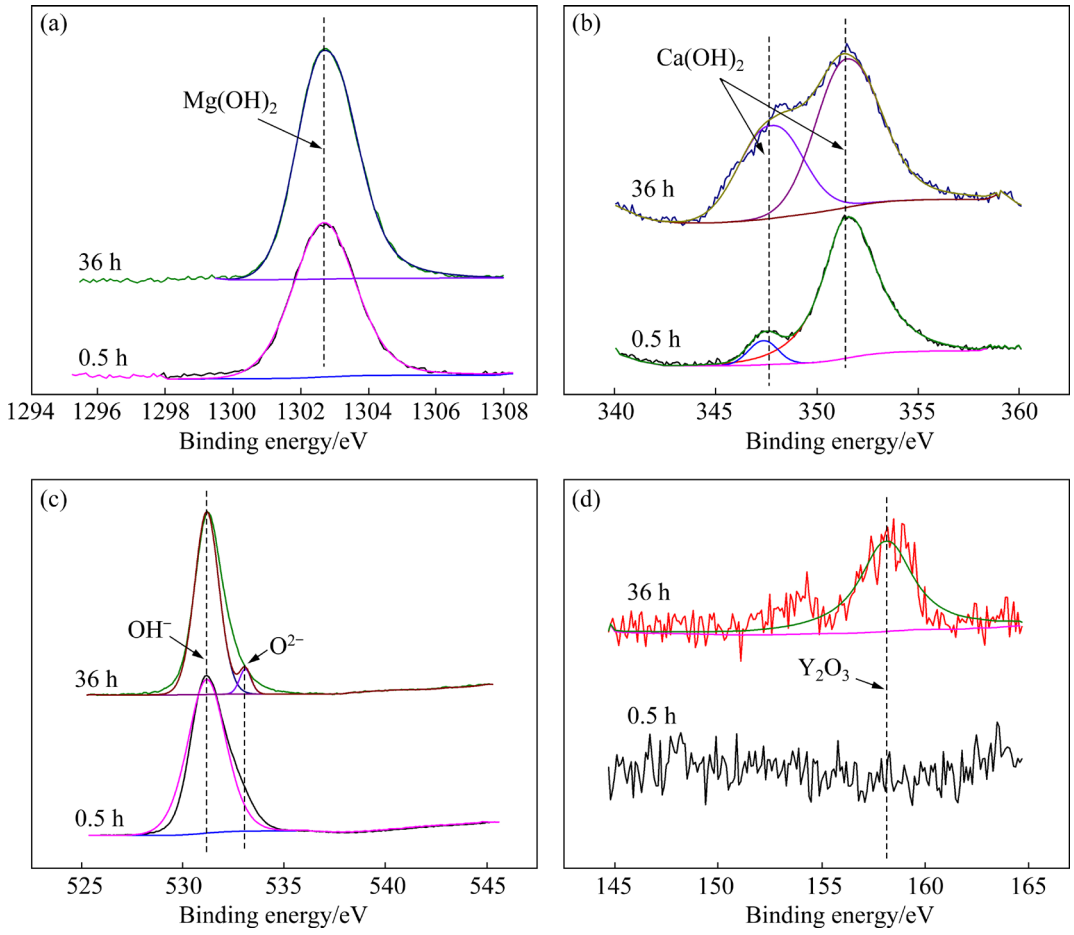

Fig. 7 High-resolution XPS results of corrosion products on surface of studied alloy after immersing in SBF solution for 0.5 and 36 h: (a) Mg 1s; (b) Ca 2p; (c) O 1s; (d) Y 3d

The fresh matrix surface is directly contacted with SBF solution to produce $Mg(OH)_2$. Meanwhile, Ca^{2+} in solution combines with OH^- to form $Ca(OH)_2$. It should be noted that the Y 3d spectrum peak at 158.5 eV suggests the existence of Y_2O_3 in the corrosion products after immersing for 36 h, which is also detected in AZ91−0.3Y alloy [28]. The atoms dissolved in Mg lattice during corrosion process produce a reaction to form Y^{3+} [19]:

$$Y \rightarrow Y^{3+}+3e \quad (9)$$

Finally, Y is oxidized to form Y_2O_3 and precipitates on the surface film to enhance the protection and improve the corrosion resistance of the alloy.

SEM morphologies of the extruded alloy after removing corrosion products and immersing in SBF solution for various time and EBSD orientation map of basal oriented grains are shown in Fig. 8. During the initial immersing period of corrosion (0.5 h), the corrosion pits could be observed on the surface, which may be related to the micro-galvanic corrosion caused by the twins and precipitate phases. Many reports [7,29] indicated that twins are crystallographic defects, which can accelerate the anodic dissolution as cathode of primary battery. And the potential difference between precipitate phases and the matrix induces the galvanic corrosion. The uncorroded area marked by the blue rectangle on the alloy surface is similar to the distribution of basal oriented grains (Fig. 8(d)). As we all know, the atomic density of (0001) is lower than that of $(10\bar{1}0)$ and $(11\bar{2}0)$ crystal planes. In general, a lower atomic density is related to a less-closely packed plane, a lower binding energy and a higher surface energy, so the corrosion rate of (0001) crystal plane is lower than that of $(10\bar{1}0)$ and $(11\bar{2}0)$ ones. Filiform-like corrosion occurs after 36 h immersion, which is mainly attributed to the formation of protective corrosion product film. The product layer containing Y_2O_3 is formed on the surface of the studied alloy when the alloy is immersed for 36 h (Fig. 7). Moreover, the Pilling−Bedworth ratio (PBR) value has been used for quantitative analysis of oxide film stress and the PBR value of protective oxide is in the range of 1−2 [30]. The PBR value of Y_2O_3 is 1.37, which confirms that the presence of Y_2O_3 is effective to prevent the pitting process from prolonging in longitudinal direction.

It should be mentioned that fall-off of grains will occur at the bottom of the filiform-like corrosion groove when immersion time is 168 h. The protection of the product film with a large number of network cracks deteriorated (Fig. 6(c)), leading to the severe galvanic corrosion between different grains with and without second phase particles. In addition, non-basal oriented grains with the volume fraction of 72.6% are preferentially corroded, which also causes severe intracrystalline

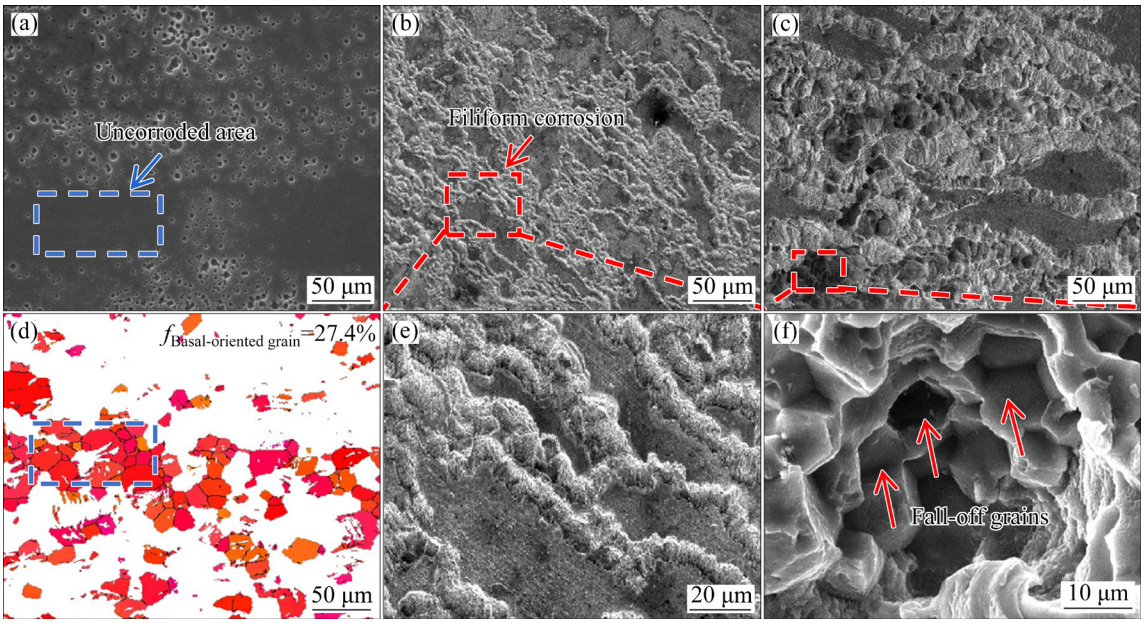

Fig. 8 SEM morphologies of extruded BWZ000 alloy after removing corrosion products and immersing in SBF solution for 0.5 h (a), 36 h (b), and 168 h (c) with high-magnification SEM images of local areas (e, f) and EBSD orientation map of basal oriented grains (d)

corrosion. The grain boundary of Mg alloys is almost cathode compared with the grain interior due to the more negative standard electrode potential [29]. In the present alloy, the grain boundary is precipitate-free region, and most of the precipitates are distributed in the grain interior. Hence, grain boundaries could provide effective barriers to corrosion process. Finally, severe variation between grain boundary and interior leads to the loose structure in BWZ000 alloy, resulting in the fall-off of grains.

3.5 Mechanical properties

Figure 9(a) shows the tensile stress–strain curve of the BWZ000 alloy. The studied alloy demonstrates UTS of 304 MPa, TYS of 237 MPa and EL of 31%. The tensile properties and corrosion behaviors of extruded Mg−0.5Bi−0.5Y−0.2Zn alloy and some previously reported extruded Mg-based alloys are summarized in Fig. 9(c). From which, the TYS of studied alloy (TYS=237 MPa) is higher than that of some other alloys containing rare earth elements (RE), such as Mg−2Y−1Zn−0.4Zr−0.3Sr (TYS=195 MPa) [31], Mg−5.3Zn−0.6Ca−1.0Ce/La (TYS=202.7 MPa) [32] and Mg−0.05Sr−0.02La (TYS=172 MPa) [33] alloys. In general, the increment in strength is also accompanied with the decrement in ductility. The TYS and EL of Mg−1.74Gd−0.5Y−1.8Zn−0.4Zr alloy extruded at 320 ℃ are 234.4 MPa and 23.8%, respectively, but, the EL increases to 26.5% with a decrease in TYS of 194.3 MPa when the extrusion temperature increases to 360 ℃ [34]. However, the studied alloy shows a better ductility (EL=31%) compared to that of the alloy with the similar strength, such as Mg−0.5Zr−1Sr (EL=6%) [35] and Mg−5Sn−3Ga (EL=21%) [36] alloys. It can be concluded that the present alloy exhibits a great synergy effect of strength and ductility. Firstly, uniform fine DRXed structure of BWZ000 alloy can improve the tensile strength by hindering the movement of dislocations. Secondly, submicron-scaled dynamic precipitation phases as shown in Fig. 2 could inhibit the movement of dislocations, leading to a certain strengthening effect. Moreover, the studied alloy has a maximum basal texture intensity of 7.39 based

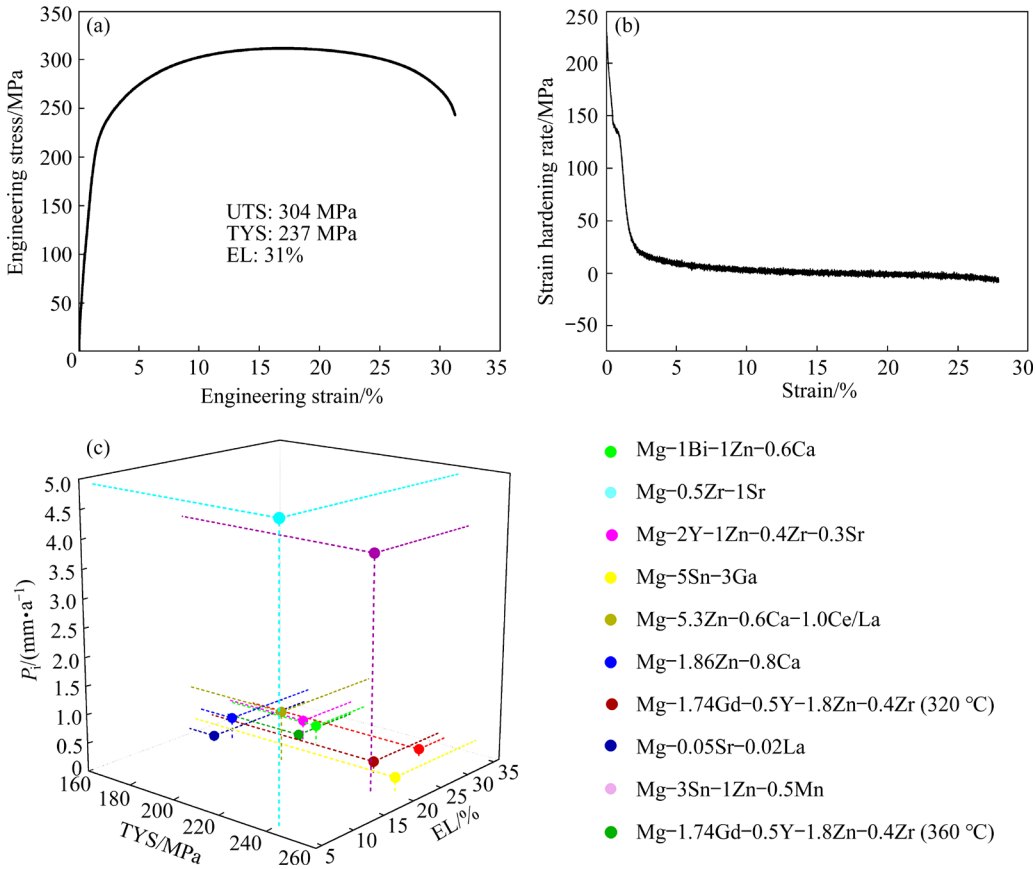

Fig. 9 Tensile engineering stress–strain curve (a), strain hardening rate versus true strain curve (b) of extruded Mg−0.5Bi−0.5Y−0.2Zn alloy and comparison of tensile properties and corrosion behavior of studied alloy with previously reported extruded Mg-based alloys in SBF solution (c)

on the (0001) pole figure shown in Fig. 1(b). The contribution of texture to TYS (σ_{tex}) can be calculated as

$$\sigma_{tex}=M\tau_0 \quad (10)$$

where M is a constant and is 6.5 times the maximum texture intensity of (0001) pole figure, and τ_0 is the critical resolved shear stress (CRSS) for the operative slip system. The value of τ_0 is 0.66, which is taken from in the extruded low-alloyed Mg−1Bi−1Zn [37]. The contribution of texture to TYS is 31.7 MPa. As we all know, the basal texture with the basal planes in most of grains preferentially orientates parallel to the ED, which makes the basal slip difficult to activate during tensile process, resulting in a strengthening effect.

Besides, based on the Hall−Petch relationship [34]:

$$\sigma_y=\sigma_0+kd^{-1/2} \quad (11)$$

where σ_y and σ_0 represent the yield strength and the material constant (21 MPa), respectively, d represents the average grain size ((10.55±1.06) μm), and k is the Hall−Petch slope (280 MPa·μm$^{-1/2}$). In the present study, the increment in TYS by grain refinement of the extruded Mg−0.5Bi−0.5Y−0.2Zn alloy is about 107.2 MPa.

In terms of ductility, fine grain structure has a higher strain coordination capability among grains, which leads to the more uniform plastic deformation. Strain hardening rate curve of BWZ000 alloy is shown in Fig. 9(b). The strain hardening rate decreases sharply at the initial stage, which is caused by a short elastic-plastic transition. Then, the extruded sample exhibits an almost steady strain hardening rate, related to dynamic recovery [38]. In order to study the work hardening ability of the whole process, work hardening exponent (n) is calculated by the following equation [39]:

$$\sigma=k_1\varepsilon^n \quad (12)$$

where σ, k_1 and ε are the true stress, strength coefficient and true strain, respectively. The n value of BWZ000 alloy is 0.51. The high n value implies the excellent uniform deformation ability.

The corrosion rate (P_i) comparison of the extruded Mg-based alloys after immersion in SBF solution is also shown in Fig. 9(c). The P_i value of studied alloy (0.14 mm/a) is lower than that of Mg−1Bi−1Zn−0.6Ca (P_i=0.32 mm/a) [37], Mg−1.86Zn−0.8Ca (P_i=0.38 mm/a) [3] and Mg−2Y−1Zn−0.4Zr−0.3Sr (P_i=0.35 mm/a) [31] alloys. Based on the above results, the extruded low-alloyed Mg−0.5Bi−0.5Y−0.2Zn alloy possesses a great balance between tensile properties and corrosion resistance.

4 Conclusions

(1) The extruded low-alloyed Mg−0.5Bi−0.5Y−0.2Zn alloy exhibits a uniform fine DRXed microstructure together with certain submicron-scaled particles mainly distributed in the grain interior, and the maximum basal texture intensity is 7.39.

(2) The corrosion modes change from pitting corrosion at the initial stage to filiform corrosion dominated after immersion for 36 h, which is mainly attributed to the formation of protective corrosion product film containing Y_2O_3. Finally, local grain fall-off at the bottom of the filiform corrosion groove occurs, which is the results of structural looseness due to the combined effects of break-down of corrosion product film, and enhances micro-galvanic corrosion effect and corrosion barrier effect induced by the grain boundary.

(3) A great synergy of strength and ductility is achieved for the extruded low-alloyed Mg−0.5Bi−0.5Y−0.2Zn alloy. Excellent tensile properties are the combined outcome of the grain boundary strengthening, texture strengthening and strong strain-hardening ability.

Acknowledgments

The authors are grateful for the financial supports from the National Natural Science Foundation of China (Nos. 51704209, 51701060, 51901153), the Natural Science Foundation of Shanxi Province, China (Nos. 201801D121088, 201901D211096), and the Science and Technology Major Project of Shanxi Province, China (Nos. 20191102007, 20191102008).

References

[1] ZENG Rong-chang, QI Wei-chen, CUI Hong-zhi, ZHANG Fen, LI Shuo-qi, HAN En-hou. In vitro corrosion of as-extruded Mg−Ca alloys—The influence of Ca concentration [J]. Corrosion Science, 2015, 96: 23−31.

[2] MA Ying-zhong, WANG De-xin, LI Hong-xiang, YANG Chang-lin, YUAN Fu-song, ZHANG Ji-shan. Microstructure,

mechanical properties and corrosion behavior of quaternary Mg−1Zn−0.2Ca−*x*Ag alloy wires applied as degradable anastomotic nails [J]. Transactions of Nonferrous Metals Society of China, 2021, 31: 111−124.

[3] BAZHENOV V E, LI A V, KOMISSAROV A A, KOLTYGIN A V, TAVOLZHANSKII S A, BAUTIN V A, VOROPAEVA O O, MUKHAMETSHINA A M, TOKAR A A. Microstructure and mechanical and corrosion properties of hot-extruded Mg–Zn–Ca–(Mn) biodegradable alloys [J]. Journal of Magnesium and Alloys, 2021, 9: 1428−1442.

[4] ZHANG Cheng, WU Liang, LIU Han, HUANG Guang-sheng, JIANG Bin, ATRENS A, PAN Fu-sheng. Microstructure and corrosion behavior of Mg−Sc binary alloys in 3.5 wt.% NaCl solution [J]. Corrosion Science, 2020, 174: 108831.

[5] WANG Xue-jian, CHEN Zong-ning, ZHANG Yu-bo, GUO En-yu, KANG Hui-jun, HAN Pei, WANG Tong-min. Influence of microstructural characteristics on corrosion behavior of Mg−5Sn−3In alloy in Hank's solution [J]. Transactions of Nonferrous Metals Society of China, 2021, 31: 2999−3011.

[6] BAO Lei, ZHANG Zhi-qiang, LE Qi-chi, ZHANG S, CUI Jian-zhong. Corrosion behavior and mechanism of Mg−Y−Zn−Zr alloys with various Y/Zn mole ratios [J]. Journal of Alloys and Compounds, 2017, 712: 15−23.

[7] ZHANG Tao, SHAO Ya-wei, MENG Guo-zhe, CUI Zhong-yu, WANG Fu-hui. Corrosion of hot extrusion AZ91 magnesium alloy: I—Relation between the microstructure and corrosion behavior [J]. Corrosion Science, 2011, 53: 1960−1968.

[8] PAN Hui, PANG Kun, CUI Feng-zhen, GE Feng, MAN Cheng, WANG Xin, CUI Zhong-yu. Effect of alloyed Sr on the microstructure and corrosion behavior of biodegradable Mg−Zn−Mn alloy in Hank's solution [J]. Corrosion Science, 2019, 157: 420−437.

[9] HU Zhi, YIN Zheng, YIN Zhou, WANG Kun, LIU Qi-dong, SUN Peng-fei, YAN Hong, SONG Hong-gun, LUO Chao, GUAN Hong-yu, LUC C. Corrosion behavior characterization of as extruded Mg−8Li−3Al alloy with minor alloying elements (Gd, Sn and Cu) by scanning Kelvin probe force microscopy [J]. Corrosion Science, 2020, 176: 108923.

[10] CHENG Wei-li, MA Shi-chao, BAI Yang, CUI Ze-qin, WANG Hong-xia. Corrosion behavior of Mg−6Bi−2Sn alloy in the simulated body fluid solution: The influence of microstructural characteristics [J]. Journal of Alloys and Compounds, 2018, 731: 945−954.

[11] ZHANG Xiao-bo, DAI Jian-wei, ZHANG Rui-feng, BA Zhi-xin, BIRBILIS N. Corrosion behavior of Mg−3Gd−1Zn−0.4Zr alloy with and without stacking faults [J]. Journal of Magnesium and Alloys, 2019, 7: 240−248.

[12] JIN S C, CHA J W, LEE J H, LEE T K, HAN S H, PARK S H. Improvement in tensile strength of extruded Mg−5Bi alloy through addition of Sn and its underlying strengthening mechanisms [J]. Journal of Magnesium and Alloys, 2021, 10: 3110−3112.

[13] LIU Yang, CHENG Wei-li, LIU Yan-hui, NIU Xiao-feng, WANG Hong-xia, WANG Li-fei, CUI Ze-qin. Effect of alloyed Ca on the microstructure and corrosion behavior of extruded Mg−Bi−Al-based alloys [J]. Materials Characterization, 2020, 163: 110292.

[14] MENG S J, YU H, FAN S D, KIM Y M, PARK S H, ZHAO W M, YOU B S, SHIN K S. A high-ductility extruded Mg−Bi−Ca alloy [J]. Materials Letters, 2020, 261: 127066.

[15] GO J B, JIN S C, KIM H J, YU H, PARK S H. Novel Mg−Bi−Al alloy with extraordinary extrudability and high strength [J]. Journal of Alloys and Compounds, 2020, 843: 156026.

[16] TOK H Y, HAMZAH E, BAKHSHESHI-RAD H R. The role of bismuth on the microstructure and corrosion behavior of ternary Mg−1.2Ca−*x*Bi alloys for biomedical applications [J]. Journal of Alloys and Compounds, 2015, 640: 335−346.

[17] LIU Yang, CHENG Wei-li, GU Xiong-jie, LIU Yan-hui, CUI Ze-qin, WANG Li-fei, WANG Hong-xia. Tailoring the microstructural characteristic and improving the corrosion resistance of extruded dilute Mg−0.5Bi−0.5Sn alloy by microalloying with Mn [J]. Journal of Magnesium and Alloys, 2021, 9: 1656−1668.

[18] CHENG Wei-li, LIU Yan-hui, ZHANG Yao, MENG Shuai-ju, ARTHANARI S, WANG Hong-xia, WANG Li-fei. Tensile properties and corrosion behavior of a dilute Mg−0.5Sn−0.7Al−0.8Zn alloy applied for biomaterials [J]. Metals and Materials International, 2021, 27(11): 4510−4516.

[19] LIU Ming, SCHMUTZ P, UGGOWITZER P J, SONG Guang-ling, ATRENS A. The influence of yttrium (Y) on the corrosion of Mg−Y binary alloys [J]. Corrosion Science, 2010, 52: 3687−3701.

[20] HE Wei-wei, ZHANG Er-lin, YANG Ke. Effect of Y on the bio-corrosion behavior of extruded Mg−Zn−Mn alloy in Hank's solution [J]. Materials Science and Engineering: C, 2010, 30: 167−174.

[21] CHENG Wei-li, TIAN Quan-wei, YU Hui, ZHANG Hua, YOU Bong-you. Strengthening mechanisms of indirect-extruded Mg−Sn based alloys at room temperature [J]. Journal of Magnesium and Alloys, 2014, 2: 299−304.

[22] YUAN Ding-ling, CHEN Song-yi, CHEN Kang-hua, HUANG Lan-ping, CHANG Jiang-yu, ZHOU Liang, DING Yun-feng. Correlations among stress corrosion cracking, grain-boundary microchemistry, and Zn content in high Zn-containing Al−Zn−Mg−Cu alloys [J]. Transactions of Nonferrous Metals Society of China, 2021, 31: 2220−2231.

[23] THAHA Y N, KARTIKA I, GEDE P A I N, LESTTARI F P, ERYANI A, ROKHMANTO F, UTOMO M S. The effects of Na_2HPO_4 on corrosion behavior of Mg−5%Zn and Mg−7%Zn alloys in ovalbumin [J]. Materials Chemistry and Physics, 2021, 273: 125112.

[24] LIU Jin-hui, HAN En–hou, SONG Ying-wei, SHAN Da-yong. Effect of twins on the corrosion behavior of Mg−5Y−7Gd−1Nd−0.5Zr Mg alloy [J]. Journal of Alloys and Compounds, 2018, 757: 356−363.

[25] WANG Li-sha, JIANG Jing-hua, LIU Huan, SALEH B, MA Ai-bin. Microstructure characterization and corrosion behavior of Mg−Y−Zn alloys with different long period stacking ordered structures [J]. Journal of Magnesium and Alloys, 2020, 8: 1208−1220.

[26] YANG Lei, SHI Yun-qiu, SHEN Liu-jie, ZHANG Er-lin, QIN Gao-wu, LU Xiao-peng, ZHOU Xiao-rong. Effect of Ag on cathodic activation and corrosion behaviour of Mg−Mn−

Ag alloys [J]. Corrosion Science, 2021, 185: 109408.
[27] LI Xiao-jing, LIU Shu-hong, DU Yong. Investigation on the corrosion resistance of the Mg−10Al−*x*Mn alloys based on thermodynamic calculations [J]. Corrosion Science, 2021, 189: 109631.
[28] LUO T J, YANG Y S. Corrosion properties and corrosion evolution of as-cast AZ91 alloy with rare earth yttrium [J]. Materials & Design, 2011, 32: 5043−5048.
[29] SUN Yue-hua, WANG Ri-chu, PENG Chao-qun, CAI Zhi-yong. Microstructure and corrosion behavior of as-extruded Mg−*x*Li−3Al−2Zn−0.2Zr alloys (*x* = 5, 8, 11 wt.%) [J]. Corrosion Science, 2020, 167: 108487.
[30] LI Chuan-qiang, HE Yi-bin, HUANG Huai-pei. Effect of lithium content on the mechanical and corrosion behaviors of HCP binary Mg−Li alloys [J]. Journal of Magnesium and Alloys, 2021, 9: 569−580.
[31] CAO Xin, ZHANG Zheng-wei, XU Chun-xiang, REN Cong-lin, YANG Wen-fu, ZHANG Jin-shan. Micro-galvanic corrosion behavior and mechanical properties of extruded Mg−2Y−1Zn−0.4Zr−0.3Sr alloys with different extrusion temperament immersed in simulated body fluids [J]. Materials Chemistry and Physics, 2021, 271: 124928.
[32] TONG L B, ZHANG Q X, JIANG Z H, ZHANG J B, MENG J, CHENG L R, ZHANG H J. Microstructures, mechanical properties and corrosion resistances of extruded Mg−Zn−Ca−*x*Ce/La alloys [J]. Journal of the Mechanical Behavior of Biomedical Materials, 2016, 62: 57−70.
[33] TANG Hong-yan, WANG Fan, LI Dan, GU Xue-nan, FAN Yu-bo. Mechanical properties, degradation behaviors and biocompatibility of micro-alloyed Mg−Sr−RE alloys for stent applications [J]. Materials Letters, 2020, 264: 127285.
[34] LIU Ya, WEN Jiu-ba, LI Huan, HE Jun-guang. Effects of extrusion parameters on the microstructure, corrosion resistance, and mechanical properties of biodegradable Mg−Zn−Gd−Y−Zr alloy [J]. Journal of Alloys and Compounds, 2021, 891: 161964.
[35] KIANI F, LIN Ji-xing, VAHID A, MUNIR K, WEN C, LI Yun-cang. Mechanical and corrosion properties of extruded Mg−Zr−Sr alloys for biodegradable implant applications [J]. Materials Science and Engineering: A, 2022, 831: 142192.
[36] WANG Xue-jian, CHEN Zong-ning, GUO En-yu, LIU Xue-qin, KANG Hui-jun, WANG Tong-min. The role of Ga in the microstructure, corrosion behavior and mechanical properties of as-extruded Mg−5Sn−*x*Ga alloys [J]. Journal of Alloys and Compounds, 2021, 863: 158762.
[37] LIU Yan-hui, CHENG Wei-li, ZHANG Yao, NIU Xiao-feng, WANG Hong-xia, WANG Li-fei. Microstructure, tensile properties, and corrosion resistance of extruded Mg−1Bi−1Zn alloy: The influence of minor Ca addition [J]. Journal of Alloys and Compounds, 2020, 815: 152414.
[38] ZHAO Chao-yue, CHEN Xian-hua, PAN Fu-sheng, GAO Shang-yu, ZHAO Di, LIU Xiao-fang. Effect of Sn content on strain hardening behavior of as-extruded Mg−Sn alloys [J]. Materials Science and Engineering: A, 2018, 713: 244−252.
[39] ZHONG Shi-yu, ZHANG Ding-fei, CHAI Sen-sen, ZHOU Jie, HUA Jian-rong, XU Jun-yao, JIANG Bin, PAN Fu-sheng. Effect of Cu addition on the microstructure, mechanical properties and degradation rate of Mg−2Gd alloy [J]. Journal of Materials Research and Technology, 2021, 15: 477−487.

挤压态低合金化 Mg−0.5Bi−0.5Y−0.2Zn 合金的腐蚀行为及力学性能

李 峰[1]，程伟丽[1,2]，余 晖[3]，王红霞[1,2]，牛晓峰[1,2]，王利飞[1,2]，李 航[1]，侯 华[4]

1. 太原理工大学 材料科学与工程学院，太原 030024；
2. 太原理工大学 新材料界面科学与工程教育部重点实验室，太原 030024；
3. 河北工业大学 材料科学与工程学院，天津 300132；
4. 中北大学 材料科学与工程学院，太原 030051

摘 要：研发一种新型低合金化 Mg−Bi−Y−Zn 合金系，该合金系在 673 K 的挤压温度下成功成型。通过扫描电子显微镜(SEM)、电子背散射衍射(EBSD)、电化学试验和拉伸试验研究挤压态合金的腐蚀行为和拉伸性能。挤压后，合金表现出几乎完全的动态再结晶组织和典型的挤压织构，在晶粒内可以观察到一些亚微米级析出相。在 SBF 溶液中，合金的腐蚀模式由最初的点蚀为主转变为中间过程的丝状腐蚀为主；最后经长时间浸泡后，腐蚀模式转变为丝状腐蚀和局部晶粒脱落。挤压态 Mg−0.5Bi−0.5Y−0.2Zn 合金的屈服强度为 237 MPa，极限抗拉强度为 304 MPa，伸长率为 31%，平均腐蚀速率为 0.14 mm/a。由此可见，该合金表现出良好的拉伸性能和耐腐蚀性能匹配度，这主要归因于其均匀的晶粒结构和亚微米级析出相。因此本文所研发的 Mg−0.5Bi− 0.5Y−0.2Zn 合金具有在生物医药领域的广阔应用前景。

关键词：Mg−Bi 基合金；挤压；腐蚀行为；力学性能

(Edited by Wei-ping CHEN)